Network Stretching, Slip Processes, and Fragmentation of Crystallites during Uniaxial Drawing of Polyethylene and Related Copolymers. A Comparative Study

R. Hiss, S. Hobeika, C. Lynn, and G. Strobl*

Fakultät für Physik der Albert-Ludwigs-Universität, 79104 Freiburg, Germany

Received November 17, 1998; Revised Manuscript Received April 13, 1999

ABSTRACT: When polyethylene (PE) is deformed to large strains, the stress originates from both the viscous forces associated with the plastic deformation of the crystallites by slip and fragmentation processes and the entropic elastic forces arising from the stretching of the entangled amorphous regions. Relative weights of the different processes change with the crystallinity. The dependencies were analyzed in a comprehensive study on a series of samples encompassing a large range of crystallinities: PE, low-density PE (LDPE), and ethylene−vinylacetate copolymers. The comparison was based on measured true stress−strain curves for constant strain rates. For the samples with higher crystallinity, which show a necking, this was achieved by employing a video-controlled tensile testing machine. Recovery properties of the sample were studied in step-cycle runs, where the load was applied stepwise and interrupted after each step by an unloading−reloading loop. Simultaneous with the mechanical testing, the related texture changes were determined by a measurement of the WAXS patterns. In spite of the large changes in the gross mechanical properties from solid- to rubberlike, there exists a common general scheme for the deformation behavior. For all samples, one finds four characteristic points where the differential compliance changes. They may be associated with (1) the onset of isolated slip processes, (2) a change into a collective activity of the slips, (3) the beginning of crystallite fragmentation, and (4) chain disentanglement resulting in a finite truly irreversible deformation. When the crystallinity is increased, the stresses at the four transition points also increase. The related strains, however, remain essentially constant. Crystal textures are also a function of the imposed strain only, the dependencies being common for all samples. Experiments support the novel picture of a granular substructure of the crystalline lamellae as a basic structural feature. Block slips with the three surfaces as slip planes enable the system to easily react on each imposed strain in a well-defined way.

1. Introduction

When polyethylene (PE) is deformed in the solid state, until fracture, it passes through a series of different structural states. For many years, studies to analyze the complex behavior have been carried out, and a broad knowledge has been accumulated. Work still continues, thus indicating that, in spite of the large number of contributions, a generally accepted overall picture has not yet been established.

In a global view, deformation of the partially crystalline polyethylene may be understood as the stretching of a network under conditions of a high, nonlinear internal viscosity. The view originates from the observation that drawn samples show an almost complete retraction to their original length when heated up to the melting point. The network is set up by the chain entanglements which act like cross-links. These are not removed by the crystallization process but just shifted into the amorphous regions. The shrinkage was dealt with, for example, in works of Capaccio and Ward[1] and Pakula and Trznadel.[2] Haward[3,4] demonstrated that the stress−strain dependencies obtained for PE and other semicrystalline polymers often equal the extension curve of an ideal rubber with viscous elements superposed. Termonia and Smith[5] devised a computer model, in which a partially crystalline polymeric solid is represented by a network of entangled chains in the presence of van der Waals bounded crystallites.

The network stretching is accompanied by characteristic changes in the texture of the crystallites, and for many authors, analysis of these changes is the main point of concern. Particularly clear results were obtained for drawn-and-rolled samples with a single-crystallike texture, when put under an uniaxial compressive force. Employing wide and small angle X-ray scattering Cowking and Rider,[6] Keller and Pope,[7] and Bowden and Young[8,9] found direct evidence for two slip processes, an interlamellar sliding and a crystallographic intralamellar slip of type (100)[001] (slip planes perpendicular to the *a*-axis, shift in chain direction). The same processes were found again in compression and shear experiments on spherulitic samples carried out by Bartczak et al.,[10,11] here also directly in TEM observations. In principle, the intralamellar slip may be accomplished by a homogeneous shearing of the layerlike crystallites or by relative displacement of blocks. Seguela and Rietsch[12] and Gerrits and Tervoort[13] propose that both types exist and become active successively.

Under a tensile force, a microscopic voiding may arise in addition to the slip processes. This occurs for lamellar stacks oriented perpendicular to the stress direction (compare, for example, a work by Petermann and Schultz[14]). When strained, fibers separated by elongated voids form within the amorphous layers. Last but not least, crystals which experience a pressure perpendicular to the chain direction may react with twinning[15,16] or with a "martensitic transition" from the orthorhombic to a metastable monoclinic phase.[17,18]

Each of the various deformation modes needs specific conditions, i.e., a favorable orientation of the crystalline−amorphous layer stack with regard to the stress field. For an isotropic PE sample with spherulitic

10.1021/ma981776b CCC: $18.00
Published on Web 06/10/1999

Table 1. Polyethylene and Related Copolymers. Properties of Samples

sample name	number of branches [CH_3/1000 C]	VA content [wt %]	melt flow index [g/10 min]	crystallinity	melting peak location [°C]
HDPE			(M_w = 390.000)	0.76	138.5
LDPE 24	24		17−22	0.50	116.9
LDPE 33	33		17−22	0.46	113.5
PEVA 12		12	0.30	0.33	97.4
PEVA 18		17.5	0.37	0.26	88.6
PEVA 27		27	3.0	0.18	76.1

morphology, these conditions change continuously with the systematically varying orientation. This was nicely demonstrated in the early work of Hay and Keller.[19] Employing polarizing light microscopy, together with micro-X-ray scattering and electron microscopy, during the cold drawing of films, they observed how the deformation of the spherulites progresses. It takes place partly homogeneously, via the inter- and intralamellar slip processes, and partly in a heterogeneous fashion, by fibrillation and voiding.

A model devised by Peterlin[20] was particularly well received and, in spite of repeated criticism, widely acknowledged. It deals with the processes active in the late stages of deformation, which finally transfer PE samples completely into a fibrillar morphology. Peterlin introduced the concept of "microfibrils" as representing the main structural element. These should form directly after the breakup of the crystallites into the already existing mosaic blocks, by aligning them, coupled by tie molecules, along the stress direction. Deformation in the later stages, shortly before fracture, should then occur by longitudinal sliding motions of the microfibrils. Criticism came from different sides. Kanig, for example, when carrying out detailed electron microscopy studies on deformed PE films through all stages, could not find any evidence for the suggested transition of one crystal lamellar into a microfibril. Rather, a network of fibers cross-linked by crystal blocks was observed.[21] As a second problem, it is found that the block thickness (along the chain direction) in the fibrillar state differs, in general, from the original crystal thickness. It depends only on the temperature of drawing; there is no memory back to the first crystallites.

Hence, looking through the literature with the multitude of works dealing with different mechanisms contributing to the deformation behavior of PE, a varied picture arises. Surely the weights and importance of the discussed processes vary with the sample properties. On the extremes, we have high-density polyethylene, showing solidlike elastic properties, and PE-based rubbers with an only low remaining crystallinity. We found it worthwhile to investigate whether both materials are also qualitatively different in their deformation behavior or still have much in common. With this aim, we carried out a study on six PEs encompassing a broad range of crystallinities, one high-density PE (HDPE), two low-density PE (LDPEs) and three ethylene−vinylacetate copolymers (PEVA).

A comparison of the deformation behavior on the basis of the usually obtained "engineering" tensile stress−strain curves alone is difficult, due to the necking. If necking occurs, in HDPE and most of the LDPEs, it strongly affects the measured stress−strain curve, and a comparison becomes impossible. G'Sell et al.[22,23] showed a way to overcome this difficulty, devising a method which enables true stress−strain curves to be measured for constant rates of straining. This is achieved by a video measurement of the neck diameter and a continuous readjustment of the cross-head speed in a feedback-loop control system. We utilized a similar experimental setup, thereby obtaining for all samples true tensile stress−strain curves which allowed for direct comparisons. Strains in polymeric samples such as PE are always composed of a recoverable and a (quasi-)permanent part. We achieved a decomposition by increasing the strain stepwise, carrying out an unloading−loading cycle after each step. Simultaneous with the mechanical testing, we determined the related structural changes by measurements of the wide angle X-ray scattering patterns.

The results presented in the following show that in spite of the large changes in the gross mechanical properties from solidlike to rubberlike behavior there exists a common general scheme for describing the deformation. We introduce and explain this scheme, discuss its micromechanical background and consider the changes of some characteristic parameters through the different samples.

2. Experimental Section

2.1. Samples. Materials for the study were supplied by BASF AG, Ludwigshafen (HDPE and LDPE) and Exxon Chemical Europe, Inc., Machelen, Belgium (PEVA). They are listed in Table 1, with some characteristic properties indicated. The crystallinities were derived from the heats of fusion.

Samples were prepared by pressing the pellets at 140 °C into sheet form. Crystallization occurred during a controlled slow cooling of the pressure plates down to room temperature (the melting peak locations given in Table 1 were determined during a subsequent heating). Film thicknesses were in the range of 0.2−0.5 mm. Samples with the "dog bone" standard form were obtained with the aid of a stamp.

The mechanical testing was carried out with an Instron 4301 tensile stress machine. Figure 1 shows engineering stress−strain curves up to fracture, measured for a constant cross-head speed (10 mm min^{-1}) for the HDPE, one LDPE, and one PEVA. The HDPE showed a pronounced, and the LDPE a weak, necking effect, as indicated by form of the related load maxima; the PEVA remained homogeneous.

2.2. Video-Controlled Tensile Testing. True stress−strain curves for constant strain rates, enabling comparison between the different samples, were obtained with the experimental setup schematically presented in Figure 2. It comes close to the device developed and used by G'Sell and his co-workers. When a neck begins to form, its profile is registered with the aid of a CCD camera. Assuming a constant sample volume during the deformation, the local strain in the center of the neck can be derived from the minimum diameter. The related local stress can be calculated simultaneously. It follows from the tensile force and the cross-sectional area at the neck center, applying in addition a correction factor

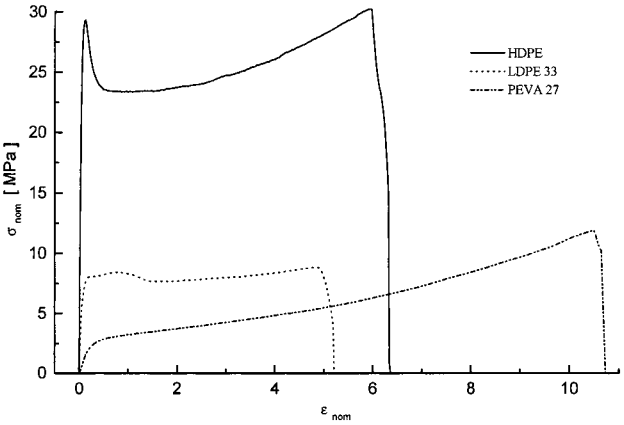

Figure 1. Engineering stress−strain curves, obtained for three samples of different crystallinity (cross-head speed: 10 mm/min).

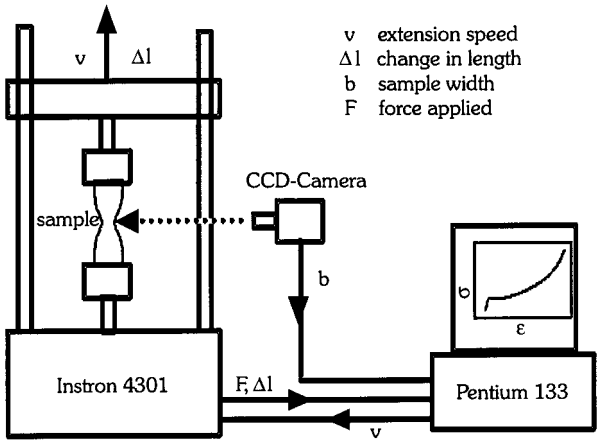

Figure 2. Video-controlled tensile testing machine: general setup.

accounting for the stress enhancement at the curved neck surface. This factor, β, has been derived by Bridgman[24] as being dependent on the diameter b and the radius of curvature R_c of the neck and reads

$$\beta = \left[\left(1 + \frac{4R_c}{b}\right)\log\left(1 + \frac{b}{4R_c}\right)\right]^{-1} \quad (1)$$

In a stretching run, the true values of stress and strain are continuously registered with the aid of the video camera connected to a computer via a frame grabber. The results are used to adjust the cross-head speed in such a way that a constant local strain rate is maintained in the center of the neck. We thereby referred to the Hencky measure of strain

$$\epsilon_H = \ln\lambda \quad (2)$$

where λ denotes the extension ratio. A constant Hencky strain rate $\dot{\epsilon}_H$ means a constant relative length change per second, resulting in an exponential length growth with time

$$\lambda = \exp \dot{\epsilon}_H t \quad (3)$$

Typical strain rates in our experiment were $\dot{\epsilon}_H = 10^{-2} - 10^{-3}\ s^{-1}$. They could be accomplished with regulation periods for the readjustment of the cross-head speed on the order of 300 ms. The task to be carried out during a period by the various sensors, moving parts, and the computer includes the measurement of the tensile force, the video registration of the profile, its digitization and evaluation to get b and R_c, the calculation of the strain and the strain rate, and the change, if necessary, of the cross-head velocity of the Instron. More technical details and information about the controlling software (written in PASCAL) and the (PID-)regulation parameter are given elsewhere.[25]

The strain imposed on a sample is generally made up of a recoverable and a remaining part. Since relaxation processes are involved, the partition depends on time and temperature; pro-longed storing and heating after the deformation generally leads to a reduction of the remaining part. We used the video control to learn about these properties, by carrying out three specific experiments. First, we observed the free shrinkage. After extending with a constant strain rate to a predetermined end strain, the lower clamp was released, and the change in the sample width was monitored. The strain equating to the amount of contraction is the reversible contribution. Second, heating the sample after shrinkage close to the final melting point causes it to shrink further. Only that deformation which is still present after heating is truly irreversible. Third, the shrinkage was carried out in a controlled fashion, performing step-cycle runs. Instead of simply releasing the lower clamp, the sample is contracted at a predetermined speed. The sample is extended step-by-step with a constant Hencky strain rate. After each step, the sample's speed of extension is inverted and used to contract the sample until a stress of zero is achieved. Thereupon, the sample is extended again, at this given speed, until it re-reaches the point at which it left the regulated curve. The amount of strain present at a stress of zero constitutes for this experiment the remaining part. The three methods yield different divisions of the total strain, each in a well-defined reproducible way.

2.3. X-ray Scattering. Analysis of the texture of the crystallites in the deformed sample was carried out by wide angle X-ray scattering experiments. Employing a Mini-Instron (Rheometric Scientific Mini Mat 2000), samples could be kept under stress during the exposure. We used a rotating Cu anode generator (Fa. Schneider, Offenburg) at the point focus and registered with an image plate detector (Fa. Schneider, Offenburg) the scattering of the (200)- and (110)-lattice planes of the PE crystallites. Scattering diagrams were obtained within minutes. The orientational distributions of the related lattice planes, $I(\theta)$, were derived from the measured intensity distributions along the Debye circles using the Polanyi equation[26]

$$\cos\theta = \cos\vartheta_{hkl}\cos\vartheta$$

The equation relates the azimuthal angle along the Debye circle, ϑ, to the angle θ between the stretching direction and the normal vector of the lattice plane (ϑ_{hkl} denotes the Bragg scattering angle).

3. Results

3.1. Controlled Stretching with a Constant Local Strain Rate. Employing the video-controlled tensile testing, we measured, for all samples, the true stress−strain dependence at a constant strain rate. Figure 3 shows the results obtained for $\dot{\epsilon}_H = 5 \times 10^{-3}\ s^{-1}$.

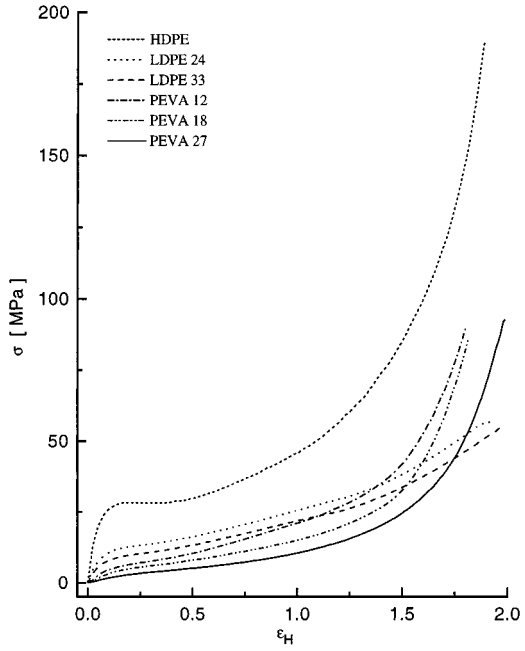

Figure 3. Relation between true stress and true strain for the five samples under study, obtained by a video-controlled stretching experiment at a constant strain rate $\dot{\epsilon}_H = 5 \times 10^{-3}$ s^{-1}. Measurements were carried out over similar ranges away from the points of fracture.

Contrasting with the different engineering stress−strain curves we now find obvious similarities between the curves, in particular those measured for HDPE and the PEVA samples; the overshoot observed in the HDPE engineering stress−strain curves has completely disappeared.

For HDPE and PEVAs, a strain hardening arises at high values of ϵ_H, whereas for the LDPE samples this does not occur. The difference may be understood from Figure 1, because the LDPE fracture occurs much earlier and this lowered fracture strength does not allow for any strain hardening. Outside of this range, for strains below $\epsilon_H = 0.7$, the change in the true stress−strain curves is systematic through all samples.

The $\sigma(\epsilon_H)$ curves depend on the imposed strain rate. As expected, the largest effects were found for the highest crystallinity, i.e., the HDPE sample. Figure 4 shows the curves measured for different strain rates, in the range between 10^{-4} and 10^{-2} s^{-1}. They essentially agree with results obtained by G'Sell.[23] Stresses increase with increasing strain rate. The dependence is indicated in Figure 5, in a comparison of the stresses measured for $\epsilon_H = 0.25$. It obeys the law

$$\sigma \approx \ln(\text{const} \times \dot{\epsilon}_H)$$

as is indicative for an Eyring rate process. It is the same dependence as that found for the drawing stress in engineering stretching experiments on partially crystalline and glassy polymers.

3.2. Step-Cycle Testing. The first method used to study recovery effects was a stepwise straining of samples interrupted after each step by an unloading−loading cycle. Figure 6 shows some typical curves obtained when employing this step-cycle test. Stresses grow during the step-by-step strain increase and follow a hysteresis loop during the unloading−reloading cycle. The results shown in the figure were obtained for the HDPE, one of the LDPE, and one of the PEVA samples,

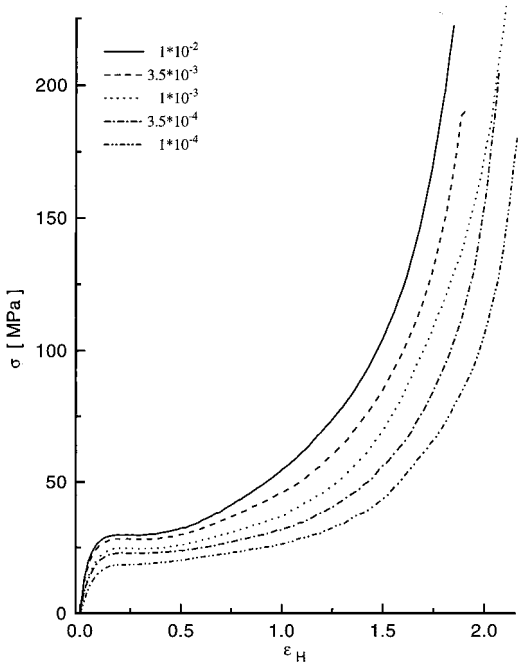

Figure 4. HDPE: True stress−true strain relations for different constant strain rates $\dot{\epsilon}_H$.

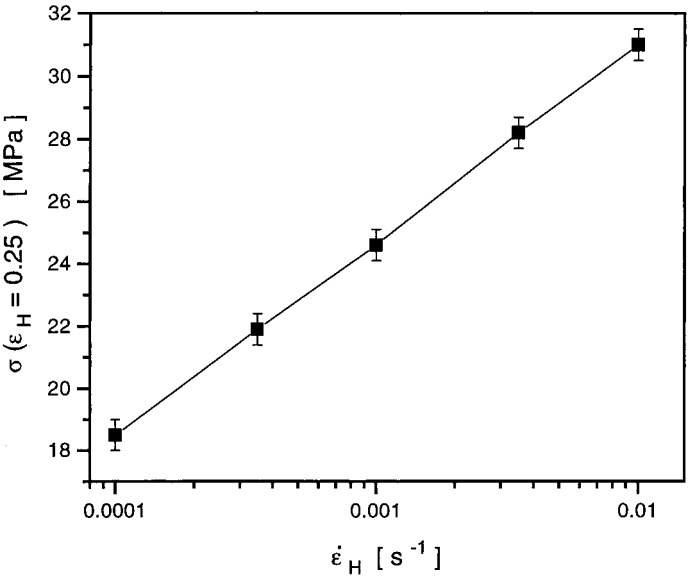

Figure 5. Data of Figure 4: drawing stress in the plateau region ($\epsilon_H = 0.25$) as a function of the strain rate.

respectively. Figures include once again the dependence of $\sigma(\epsilon_H)$, measured during a continuous stretching with the same rate, $\dot{\epsilon}_H = 5 \times 10^{-3}$ s^{-1}. As the comparison shows, the stepwise stretching interrupted by the cycle, always comes back to the continuous curve. Hence, no structure change or irreversible flow occurs during the cycling time, and the cycle amplitude indeed yields the recoverable part of the strain also during a continuous stretching. One observes characteristic differences between the three samples. The strain recovery on unloading is only small for the HDPE and then increases with decreasing crystallinity. PEVA is associated with the largest recoverable strain.

The experimental results enable the total strain to be split in two parts, a recovered one, $\epsilon_{H,c}$, describing the strain associated with the cycle, and a second one, the "base part" $\epsilon_{H,b}$, giving the strain remaining in the

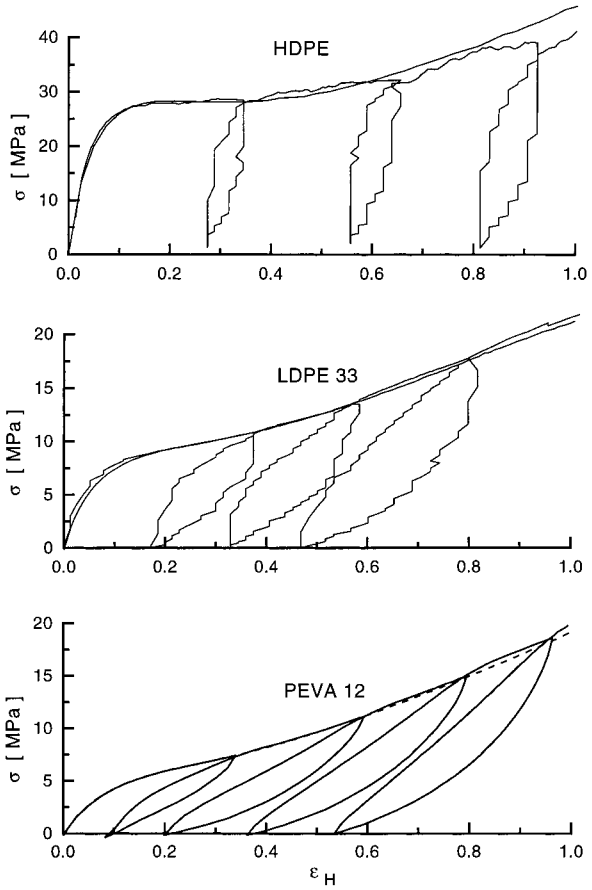

Figure 6. Step-cycle tests carried out for HDPE, LDPE33, and PEVA12. Comparison with the noninterrupted constant strain rate run ($\dot{\epsilon}_H = 5 \times 10^{-3}$ s^{-1}).

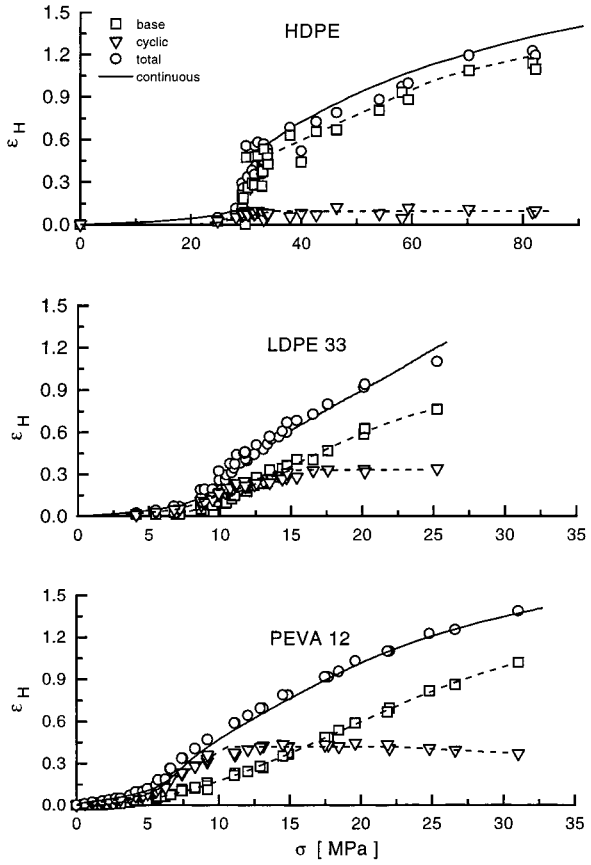

Figure 7. Evaluation of step-cycle tests on HDPE, LDPE33, and PEVA12: partitioning of the total strain ϵ_H into the strain amplitude of the cycles $\epsilon_{H,c}$ and the strain which remains in the moment of complete unloading $\epsilon_{H,b}$.

moment of complete unloading. Hence, we write

$$\epsilon_H = \epsilon_{H,b} + \epsilon_{H,c} \tag{4}$$

Note that the addition of two Hencky strains means that two relative length changes are added up successively, with the first one referring to the original length and the second one referring to the already extended sample. Results of the decomposition, taken from numerous step-cycle runs, are shown in Figure 7, where ϵ_H, $\epsilon_{H,c}$, and $\epsilon_{H,b}$ are shown as a function of the true stress. Again the figure also includes the $\epsilon_H(\sigma)$ dependence for comparison, measured in uninterrupted runs with the same strain rate.

Figure 8 displays the deformation behavior at the beginning, i.e., at low stresses, as obtained for PEVA12. As can be seen, this sample shows an ideal Hooke elasticity up to a strain $\epsilon_H = 0.025$ and a stress $\sigma = 1.8$ MPa. For higher extensions, strains are no longer completely recovered during the cycle.

Both the cyclic and the base component increase with increasing stress. However, as shown by Figure 7, for the cyclic part, this increase is limited, and a maximum value is reached. Interestingly, for all three samples, the plateau value of $\epsilon_{H,c}$ is reached at about the same value of the total strain, $\epsilon_H \approx 0.6$. From this strain upwards, further extension is exclusively due to an increase of the nonrecovered component.

As is demonstrated by the opening of the cycles, the recoverable part of the strain is also associated with internal friction. This internal viscosity increases with the crystallinity and with the strain rate. Results

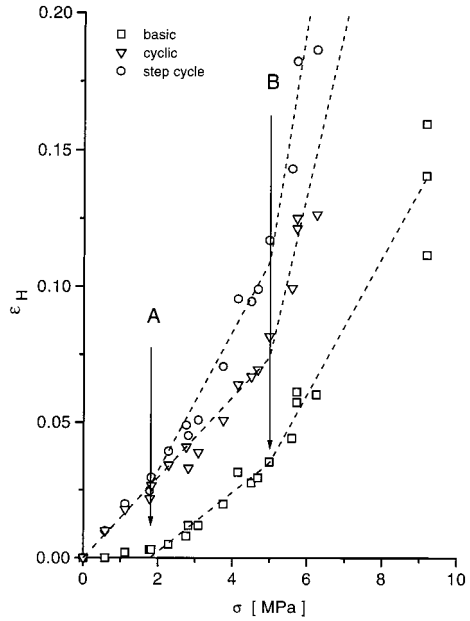

Figure 8. PEVA12: partitioning of the total strain at low deformations.

obtained in the case of PEVA12 for varying strain rates are depicted in Figure 9. The loop opening increases with increasing strain rate. Somewhat surprisingly, this change is not accompanied by measurable changes in the cyclic strain amplitude $\epsilon_{H,c}$. The maximum opening of the hysteresis curves can be used as a measure for the viscous stress and Figure 10 shows its dependence

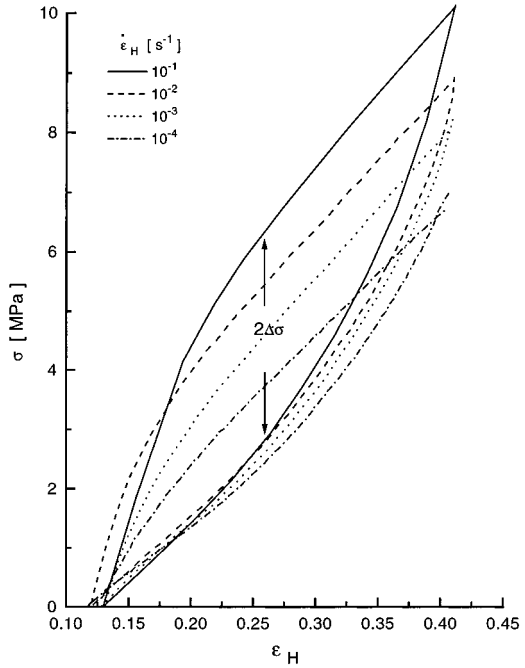

Figure 9. PEVA12: cycles after a straining to $\epsilon_H = 0.4$. Experiments conducted with different strain rates.

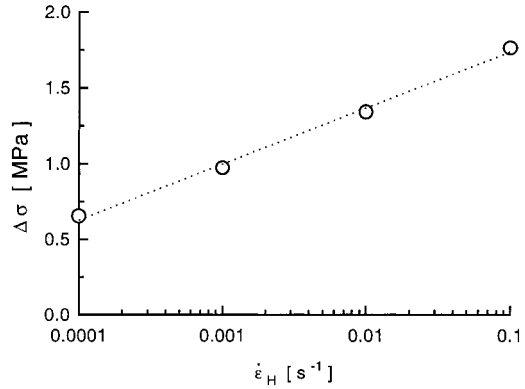

Figure 10. Data of Figure 9: viscous stress as a function of the strain rate, taken as the half value of the openings in the centers of the hysteresis cycles.

on the applied strain rate. One again observes the behavior of an Eyring rate process. As expected, comparison shows that internal viscosities in this rubberlike sample are much smaller than those found for HDPE (Figure 5).

3.3. Free Shrinkage Tests. As a second experiment in the study of the recovery effects, we used the video equipment to follow in real-time the shrinkage of samples subsequent to a release of the lower clamp. Samples were strained to various endstrains before this abrupt unloading. Figure 11 shows as an example shrinkage processes observed for LDPE33 after a straining with a strain rate $\dot{\epsilon}_H = 10^{-2}$ s^{-1}. One notes in the first moment a very rapid shrinkage which cannot be resolved by the apparatus and then, over longer periods, further slow retractions. After 5 min, the changes were already very slow, and we registered the shrinkage after 10 min. The results of these experiments, which were carried out for all samples, again yield a partition of the total strain into two parts, $\epsilon_{H,s}$, associated with the shrinkage, and $\epsilon_{H,r}$, representing the nonrecovered part. Figure 12 shows the two parts for three of the samples, now presented as a function of the total strain. The

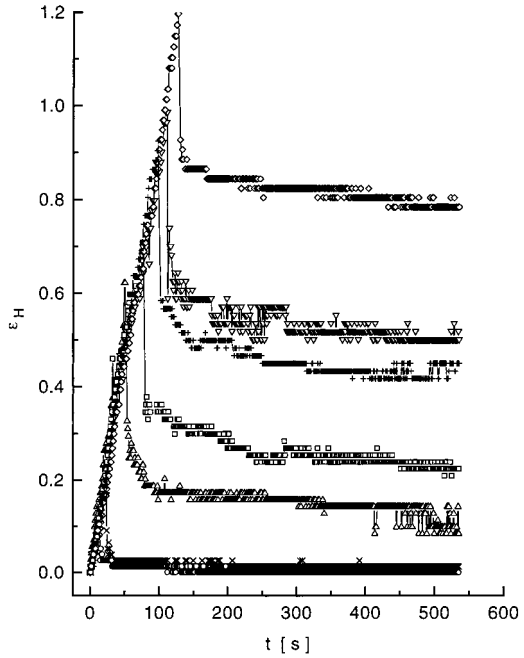

Figure 11. LDPE33: free shrinkage on unloading after different amounts of straining, as registered by the video camera.

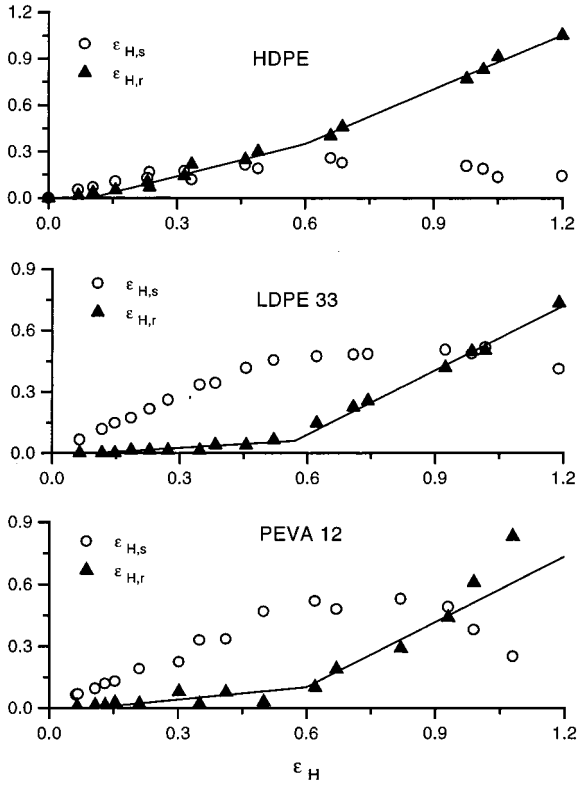

Figure 12. Evaluation of free shrinkage curves obtained for HDPE, LDPE33, and PEVA12: partitioning of the total strain into the amount of shrinkage, $\epsilon_{H,s}$, and the remaining part, $\epsilon_{H,r}$.

recovered part of the strain reaches a plateau as in the first experiment, and again, this occurs for all samples commonly, at a total strain $\epsilon_H \approx 0.6$. There is a characteristic difference in the relative weights of $\epsilon_{H,s}$ and $\epsilon_{H,r}$, when comparing HDPE with the samples of lower crystallinity, LDPE and PEVA. For the latter ones, the recovered part dominates the strain up to values of $\epsilon_H \approx 0.6$. There, the nonrecovered part starts

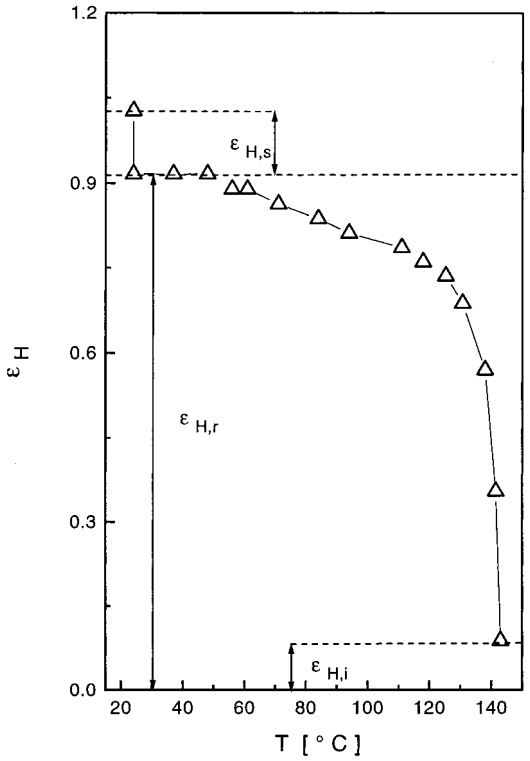

Figure 13. Shrinkage on unloading supported by heating observed for HDPE: strain as a function of temperature. The amount of spontaneous shrinkage, $\epsilon_{H,s}$, the remainder at room temperature, $\epsilon_{H,r}$, and the truly irreversible plastic deformation found at the highest temperature, $\epsilon_{H,i}$, are indicated.

to increase and finally, above $\epsilon_H \approx 1.0$, becomes dominant. Contrasting with this behavior, both parts begin in HDPE with similar weights. When the plateau in $\epsilon_{H,s}$ is reached, at $\epsilon_H \approx 0.6$, the continuing increase of the nonrecoverable part results in a dominance from there on.

In the third experiment, samples, after having let them shrink freely, were slowly heated up to temperatures in the melting range. This resulted in a further retraction. Figure 13 shows, as a typical result, observations on HDPE. After a controlled straining up to $\epsilon_H = 1.05$, the release of the lower clamp resulted in a first length reduction down to $\epsilon_H = 0.9$. Heating was then started, proceeding as indicated by the continuous line. This was accompanied by a second large amount of shrinkage, leading finally to only a small value of the remaining strain, $\epsilon_H = 0.07$. This value now corresponds to a truly irreversible plastic flow. Figure 14 collects all values of the irreversible strain, $\epsilon_{H,i}$, thus obtained. Indeed, there was no irreversible component at all for strains below $\epsilon_H \approx 0.9$. Here, heating resulted in a complete retraction. Above this critical value, one observes a steady increase of $\epsilon_{H,i}$.

Comparing the results of the three recovery experiments, we find the expected tendency: the amount of shrinkage after the deformation depends on the time given and the temperature. We have for the remaining part

$$\epsilon_{H,i} < \epsilon_{H,r} < \epsilon_{H,b} \tag{5}$$

3.4. X-ray Texture Analysis. Figure 15 collects some wide angle X-ray scattering diagrams registered for HDPE and PEVA12 at different stages of deformation (the LDPE samples yielded similar results). In the case

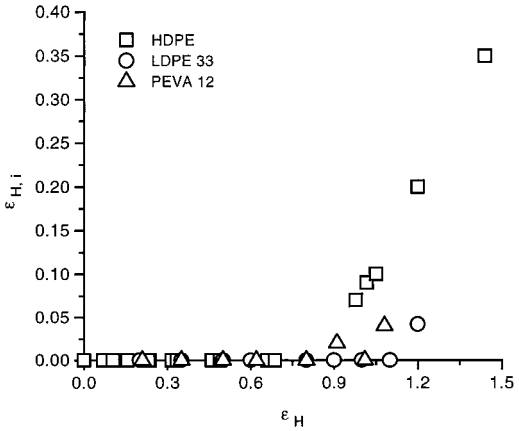

Figure 14. Nonrecoverable part of the strain $\epsilon_{H,i}$ remaining in the samples after heating.

of the HDPE, pictures were taken with a primary beam crossing through the center of the neck. After the controlled stretching to various endstrains, the samples were unloaded before transferring them into the WAXS camera for exposure. In the case of the PEVA, samples were kept under load during the measurement.

The two circles which show up in the WAXS patterns are associated with a scattering of the 200- (outer circle) and the 110- (inner circle) lattice planes. The additional scattering at smaller angles, arising for HDPE at higher deformations, originates from the monoclinic phase.

A comparison shows that both samples experience similar changes in their crystal texture. The intensity distribution apparently changes in two steps. At first, starting from the isotropic intensity distribution, broad maxima develop. For the 200-reflection, they are located on the equator (the strain is horizontally directed); for the 110-reflection, they are at an oblique angle (compare the patterns obtained for $\epsilon_H = 0.25$ and 0.50). The second step is the introduction of a new component characterized by sharp maxima for both reflections on the equator. Figure 16 depicts, as a typical result, the orientational distribution function $I(\theta) \sin \theta$ associated with the 110-lattice planes, measured for PEVA12 at a strain $\epsilon_H = 0.85$. The crystal texture here obviously corresponds to a superposition of two different ensembles of crystallites, belonging to a "lamellar" and a "fibrillar" part of the structure. To obtain the respective fractions, we carried out a decomposition on the basis of Lorentzian functions, choosing a narrow symmetric one for the fibrillar part and a broader asymmetric one (set together of two different halves) for the lamellar contribution. Figure 17 shows the fractions of the two parts as obtained for PEVA12. First indications for the occurrence of the fibrillar components are found around $\epsilon_H = 0.6$. The results obtained for HDPE are quite similar and indicative for a first formation of fibrils around $\epsilon_H = 0.6$.

A convenient measure, often used to express quantitatively degrees of orientation in uniaxially oriented samples, is the orientational order parameter defined by

$$S = \frac{3\langle \cos^2 \Theta \rangle - 1}{2} \tag{6}$$

where Θ denotes the angle enclosed by the axis of interest and the unique axis. We can use this parameter to quantify the degrees of orientation of the two lattice

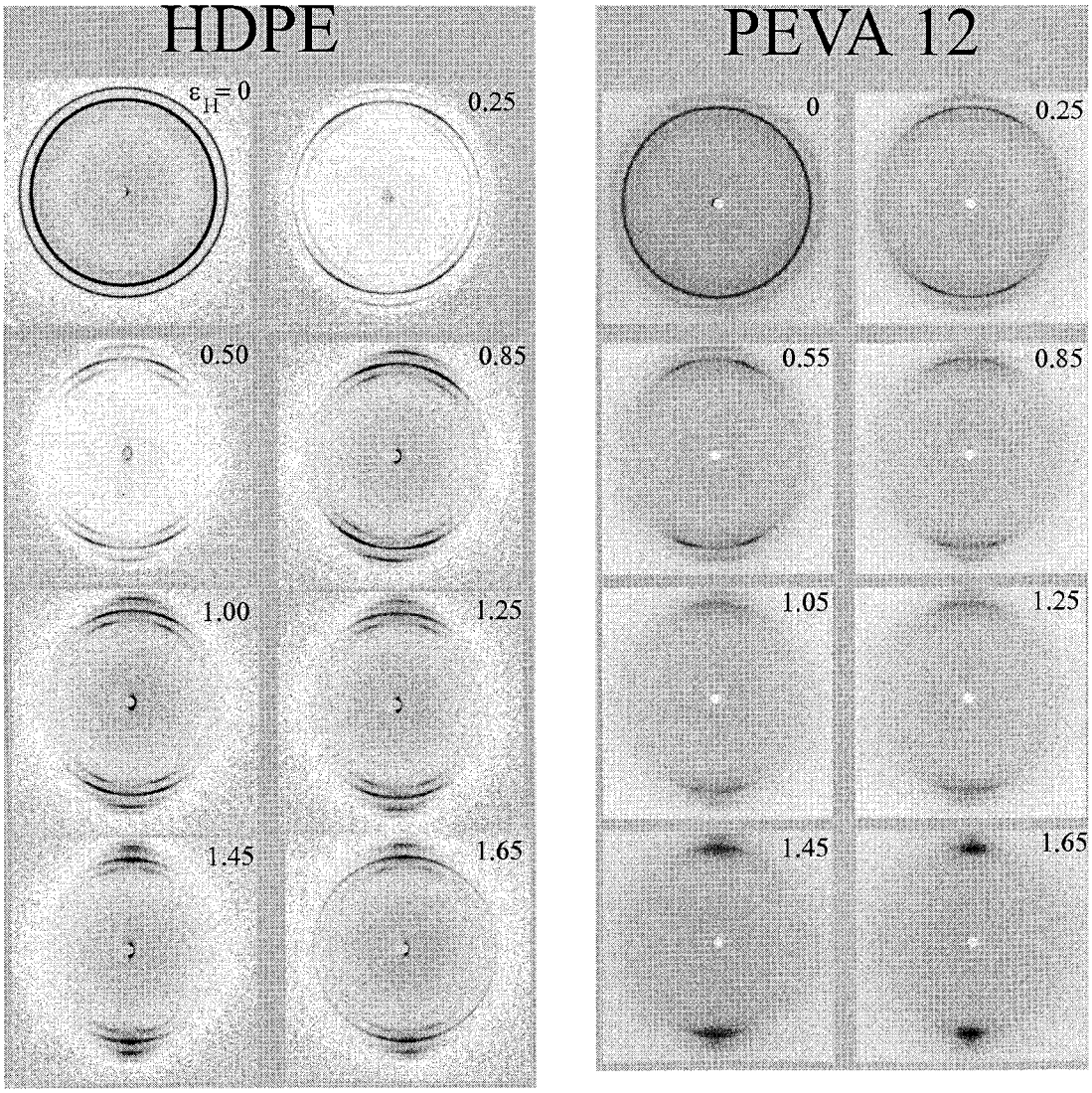

Figure 15. HDPE and PEVA12: WAXS diagrams measured for the indicated local Hencky strains, directed horizontally. Scattering patterns for HDPE were always obtained in the center of the neck.

planes (200) and (110), referring to the respective normal vectors. The values for S_{200} and S_{110} may be derived from the orientational distribution functions $I(\theta)$ of the respective lattice planes. Figure 18 gives the results thus obtained for HDPE and the three investigated samples of PEVA. For a perfect orientation of the lattice planes, with their normals in the plane of the equator, the order parameter becomes $S = -0.5$. Figures indicate that this is the limiting value for both the 200- and 110-lattice planes, the approach being more rapid for the 200-planes. Surprisingly one observes a common behavior for the strain dependencies of S_{110} and S_{200}. All of the samples, which greatly vary in their crystallinity, follow within the error limits of the measurements the same curves.

The data depicted in Figure 18 were obtained during a stepwise straining of the samples. Figures 19 and 20 show results obtained for step-cycle experiments on PEVA 12. They are surprisingly simple. As it turns out, there exists a one-to-one correspondence between the orientational order and the strain, independent of the way the strain was achieved and of whether the sample is stressed or unloaded. Figure 19 compares the intensity distributions of the 110-reflection measured at $\epsilon_H = 0.25$ during stretching (left) and at the stress free end of a hysteresis loop, which started at $\epsilon_H = 0.53$ and ended at $\epsilon_H = 0.25$ (right). Both distribution functions are equal to each other. Figure 20 collects S_{110}-values obtained for the two end points of various hysteresis loops, showing a general agreement between the S_{110}-(ϵ_H) relations for deformed samples under stress (open symbols) and in stress-free states (filled symbols).

4. Discussion

4.1. A Common Scheme Describing the Deformation Behavior. It is convenient to begin the discussion by considering the behavior of PEVA12 which produced particularly clear results. We first look at the results of the step-cycle tests given in Figures 7 and 8, in addition to Figure 21, where the focus is on the cyclic component, which is presented there in enlarged scale. Regarding these curves, one can say that during deformation the sample passes through five different regions, with cross-overs at four specific points denoted A−D. At first, there is the range of lowest strains and stresses, extending up to A (Figure 8). Here, we find an ideal Hooke elasticity. Around A conditions change. From there on, a remaining base part in the strain is registered, and the differential compliance $d\epsilon_H/d\sigma$ increases. The next change takes place around B. One

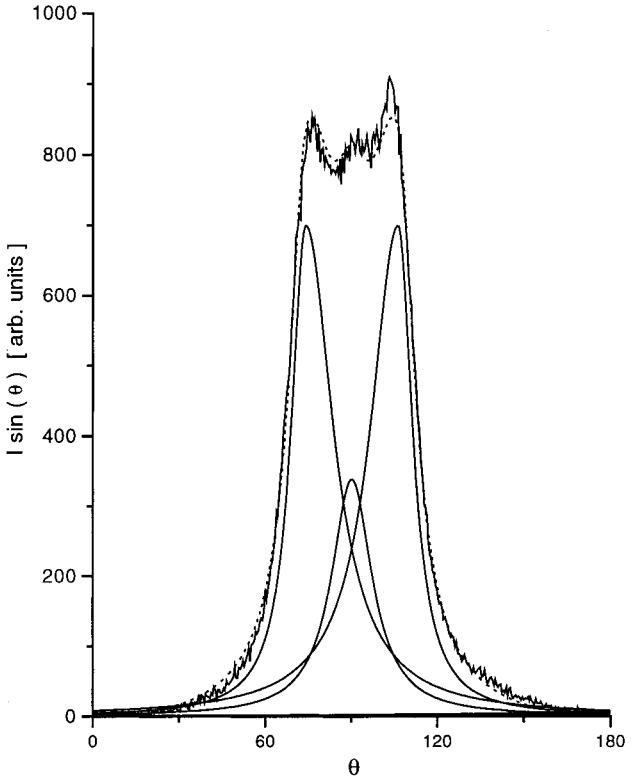

Figure 16. PEVA12, $\epsilon_H = 0.85$: orientational distribution of the 110-lattice planes $I(\theta)$ sin θ (θ is the angle between the lattice plane normal and the tensile axis), and decomposition into a lamellar and a fibrillar contribution.

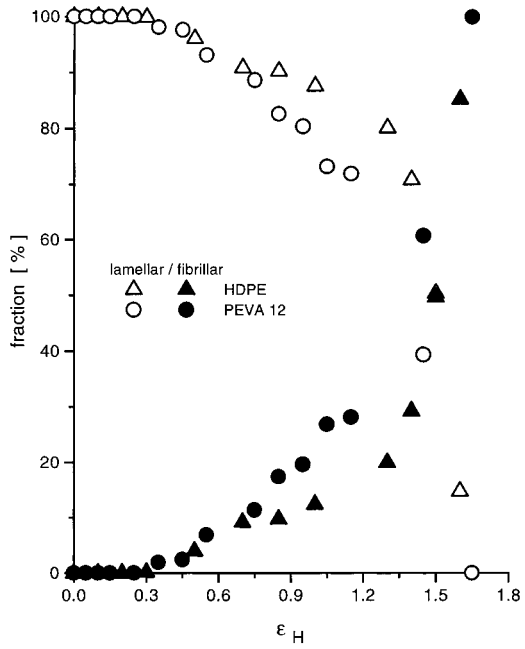

Figure 17. PEVA12: changes of the fractions of the fibrillar and the lamellar component with the strain.

observes a further, now quite pronounced, increase in the differential compliance. As shown by Figure 8, this increase originates from both the cyclic part of the differential compliance $d\epsilon_{H,c}/d\sigma$ and the base part $d\epsilon_{H,b}/d\sigma$. So far, the cyclic part of the strain has steadily increased. This comes to an end when reaching the next cross-over point, C, where $\epsilon_{H,c}$ takes on a plateau value, while the differential compliance $d\epsilon_H/d\sigma$ decreases. The plateau region for $\epsilon_{H,c}$ ends at the fourth characteristic

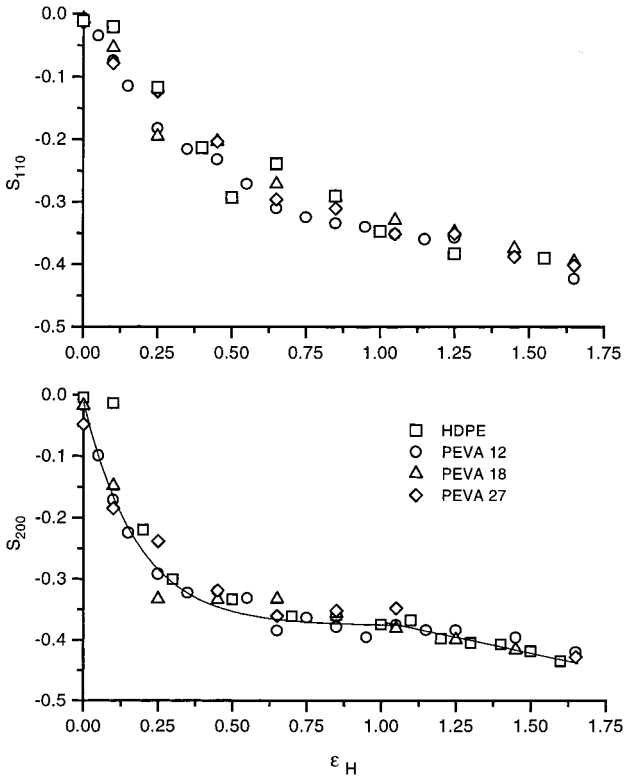

Figure 18. HDPE and PEVAs: orientational order parameters associated with the 110- and 200-lattice plane as a function of strain.

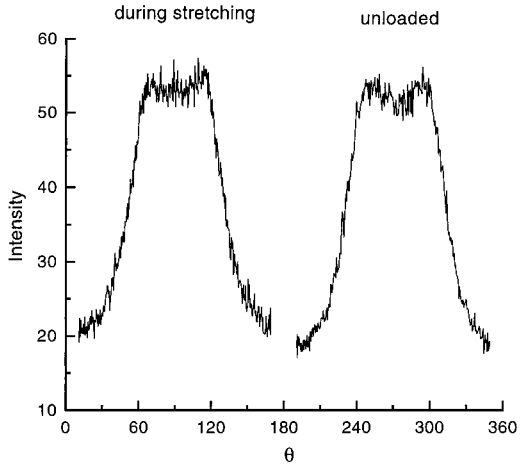

Figure 19. PEVA27 at $\epsilon_H = 0.25$: 110-orientational distributions measured during stretching and for an unloaded strained sample.

point, D, where $\sigma = 22$ MPa, $\epsilon_H = 1$ (Figure 7). It is associated with a decrease in the cyclic part of the strain and a further decrease in the differential compliance. The major characteristics of this point become apparent from Figure 14. Up until point D, there was no true plastic flow; a complete retraction on prolonged storage and heating of a sample is always found. From point D onwards, an irreversible deformation arises.

Hence, we find five regions which differ in their deformation behavior. The locations of the cross-over points are $\epsilon_H \approx 0.025$ (A), ≈ 0.1 (B), ≈ 0.6 (C), and ≈ 1.0 (D). When examining Figure 12, one notes that the transition points B−D also show up in the free shrinkage experiment. In particular, one again observes the plateau, now for $\epsilon_{H,s}$, extending between 0.6 and 1.

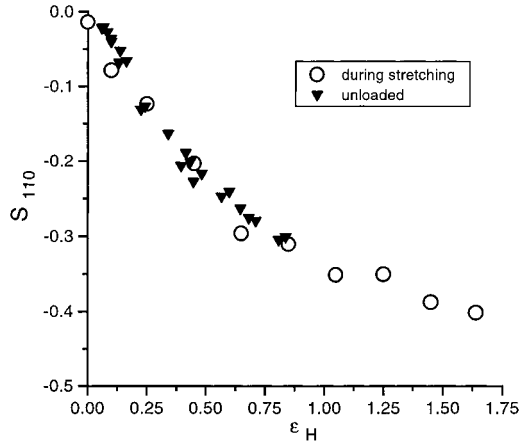

Figure 20. PEVA27: 110-order parameter in dependence on strain, measured for stressed and stress-free states during step-cycle experiments.

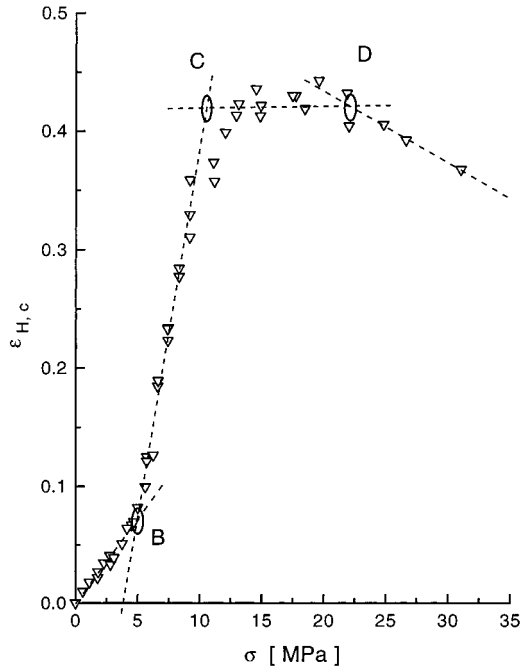

Figure 21. PEVA12: cyclic component of the strain $\epsilon_{H,c}$ dependent on the stress (enlarged view from Figure 7). Different ranges with transition points B, C, and D are indicated.

Important information comes from the X-ray scattering diagrams. As shown in Figure 17, the beginning of the plateau region, i.e., at C, is exactly where fibrils show up for the first time. Their formation leads also to a further decrease in the order parameter S_{l10} (Figure 18).

Having introduced this scheme, we now compare the different samples. The result is surprisingly simple: one finds for all samples the characteristic five regions, and furthermore, the transitions take place at similar values of ϵ_H throughout. One always observes two breaks in the differential compliance, the first one leading to an increase and the second one leading to a decrease, and they are located throughout at $\epsilon_H \approx 0.1$ (B) and ≈ 0.6 (C). The second transition may generally be associated with the appearance of the fibrils in the X-ray scattering pattern. There are further similarities; one always finds that the Hooke range ends at a strain between 0.02 and 0.03, and truly plastic flow arises only if strains reach values of more than $\epsilon_H = 1$. Figure 22 depicts these

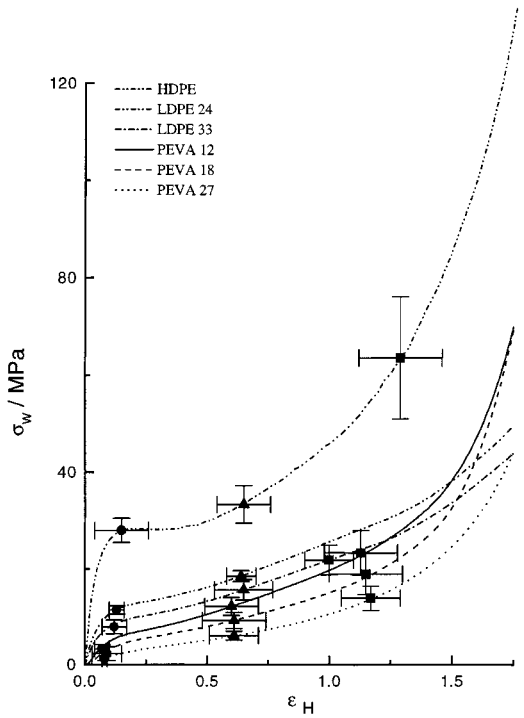

Figure 22. Locations of the transition points B−D along the true stress−strain curves measured for the different samples.

reasonably constant locations of the cross-over points, incorporated into the true strain−stress curves.

4.2. Slip Processes. On the basis of existing knowledge about the various processes contributing to the deformation of polyethylene, it is not difficult to interpret the general behavior and see the physical background of the different ranges. We shall add some comments and use our data to clarify some points under discussion.

Regarding the measured X-ray scattering patterns, it is clear that up to point C the crystal texture changes by slip processes only. The formation of fibrils subsequent to the fragmentation of the crystallites has a clear signature. They produce a sharp maximum at the equator and these contributions show up only for strains above C. There are two sorts of slip processes in the system, interlamellar shear and slips within the crystalline lamellae, mostly associated with shifts along the chain direction. As interlamellar shear leads to a deformation of the amorphous intercrystalline layers only, one might consider it as representing the easier process and therefore think that it is favored and sets in prior to the intralamellar slips. The X-ray scattering experiments allow this expectation to be checked because the texture changes resulting from inter- and the intralamellar slips are quite different. Figure 23, which represents the two slip processes in a schematic drawing, may serve for an explanation. When initiated by a tensile stress, slip processes are generally composed of a simple shear followed by a rotation of the shearing direction towards the tensile axis. The sketch indicates that inter- and intralamellar slips differ in the resulting reorientation of the chain axis. For interlamellar shears, the chain axis moves towards the equator, which implies the formation of an intensity maximum for the 100- and 010-reflection on the meridian. On the other hand, for intralamellar slips, the chain axis changes its direction towards the meridian. As a consequence, the intensity maxima of the 100- and 010-lattice planes shift towards

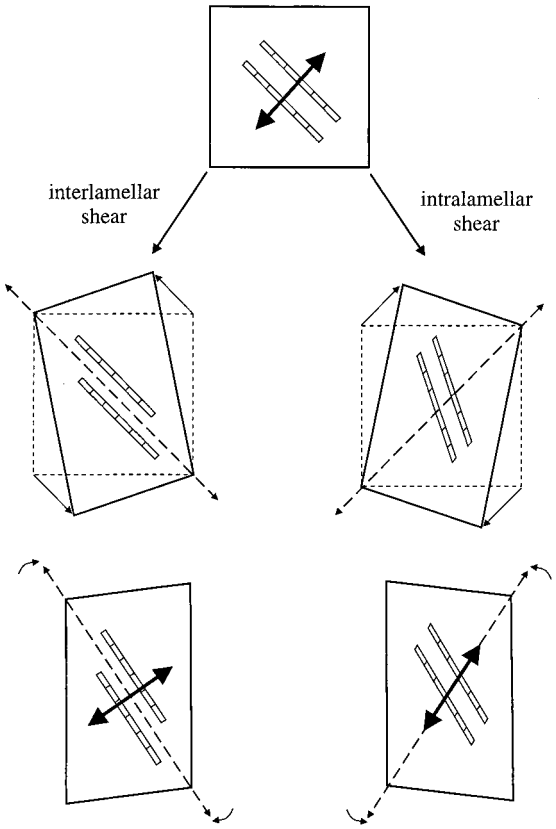

Figure 23. Extension of a sample under tensile stress via an inter- or an intralamellar slip process: simple shear combined with a rotation of the shear direction towards the axis of the stress. The two processes lead to opposite reorientations of the *c*-axis.

the equator. Hence, we have opposite tendencies for the two processes. What is the observation? Clearly, there are no signs at all for the formation of an intensity maximum at the meridian. For the 100-reflection, the maximum forms, from the very beginning, at the equator; for the 110-reflection, it shows some oblique orientation (Figure 15). These observations can only be understood if there exist from the beginning intracrystalline slip processes. To understand this behavior, one should remember the spherulitic structure of the sample with stacks of layerlike crystallites being oriented in all directions. Only in special cases, for orientations of 45° against the unique axis, the extension could be accomplished by interlamellar slip processes only. For all other orientations of lamellar stacks, a combination of different slip processes is necessary and therefore enforced. Spherulites retain their integrity up to the onset of fibrillation, and this is only possible if all of their parts react commonly in achieving the imposed uniform extension. Interlamellar shear alone would certainly be insufficient.

The situation may be different for a uniformly oriented sample. Indeed, Young and Bowden[8] when studying the texture changes of a preoriented sample under uniaxial pressure had evidence for a successive onset of the two kinds of slip processes, initially the interlamellar slips followed by the intralamellar slips. For an isotropic sample separation, this is obviously impossible.

As was repeatedly pointed out in the literature, the (100)-plane is preferred for intralamellar slips. This preference could well be the reason for the different textures observed for the (100)- and the (110)-lattice planes. Motion of the (100)-normal vector towards the equator is obviously easier than a corresponding motion of the (010)-normal vector, indicating that, as was already pointed out long ago by Hay and Keller,[19] reorientation of the chain axis around the *b*-axis occurs more readily than around the *a*-axis.

Slips are initially activated at the point A, where for the first time a small long-living strain component $\epsilon_{H,b}$ is observed. Slips thus being already activated, one may wonder about the physical origin of the further change taking place at B. As a possible view one might think that up to B slip processes occur only individually in localized zones and that B then brings a "breakthrough" to a collective flow behavior. Authors discussing the yielding of amorphous polymers came up with qualitatively similar ideas. Deformation is assumed to begin with shear transformations within isolated microdomains. With growing numbers, these deformation zones increasingly stabilize each other against the elastic backstresses of the nondeformed surroundings, which finally leads to a cooperative action and a macroscopic plastic flow. The evolution of strain in a partially crystalline way, based on slip processes, may well evolve in a similar way, starting with localized events and then changing to a common activity.

As comparison shows, the force maximum in the engineering stress−strain curve corresponds to B rather than to A. For the majority of workers this force maximum represents the "yield point" of the material, which therefore has to be associated with this breakthrough. In fact, one can also use the term yield point for the point where plastic deformation processes set in and this would be A. A helpful statement is included in a paper of Fotheringham and Cherry.[29] They distinguish between a "nucleation controlled yield point" and a "velocity controlled yield point". The first is associated with the activation of local centers of plastic flow, and the second is associated with the situation where the increasing strain essentially becomes due to the plastic part of the deformation. Clearly, our A corresponds to the nucleation controlled yield point and B to the velocity controlled point.

In recent time, one repeatedly finds reports and discussions in the literature about the occurrence of "double yield points" in polyethylene.[12,30] The feature is found in engineering stress−strain curves of low-density polyethylenes and other species of comparable crystallinity. The LDPE stress−strain curve shown in Figure 1 is a typical case. Showing after the first yield point another broad maximum, this may suggest on first view the successive onset of two different mechanisms of plastic deformation. Authors in the literature give varying assignments, for example, a block slip followed by a homogeneous block shearing[12] or interlamellar shear followed by a block slip.[30] If these kinds of interpretations are correct, the two processes should also show up in the true stress−strain curves. There, one would expect two characteristic points where the differential compliance increases, with the first process leading to the first increase and the second to an additional one. Looking on our results, a problem comes up: only one increase is observed, namely, the one located at B, and there is no second additional one. At C, there is a decrease rather than an increase, i.e., this transition leads to a strain hardening. Hence, what could be the reason for the observed broad maximum

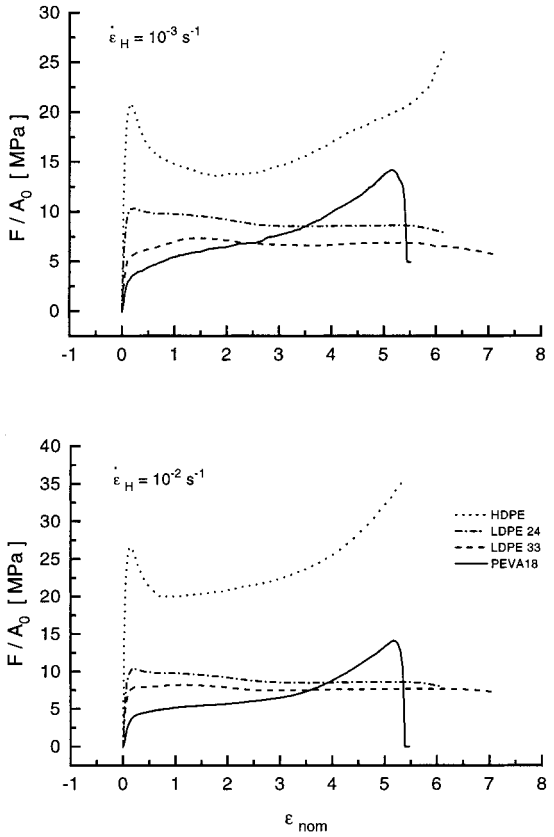

Figure 24. Dependencies between nominal values of stress and strain, as derived from measured true stress−strain curves.

in the engineering stress−strain curve of LDPE? The answer is given in Figure 24. Here, we just derived from measured true stress−strain curves the corresponding load-extension curves, writing

$$F/A_0 = \sigma/\lambda = \sigma \exp - \epsilon_H$$

where F gives the load and A_0 denotes the initial sample cross section. The results refer to two different strain rates and four different samples. As we see, in the case of LDPE , after the break located at B, there arises a second broad maximum, which, however, has no association to another specific mechanism of plastic flow. It just arises from the form of the $\sigma(\epsilon_H)$ curve. If the stress does not increase rapidly enough to compensate for the sample narrowing, a decrease in the force may arise, and this is the case for LDPE. Typically, the double yield is not observed for HDPE which has another $\sigma(\epsilon_H)$ curve.

The derived load-extension curves also provide some indication whether a sample will neck or remain homogeneous during an engineering straining test. As discussed by Vincent[31] (compare also Strobl[32] and Bernstein and Zapas[33]), necking expresses the occurrence of a mechanical instability. It exists if, within a limited range, the force decreases rather than increases with increasing extension. This is obviously the case for HDPE and is not true for PEVA. One therefore would understand that HDPE necks and PEVA does not. Conclusions based on these calculated curves, however, are not strict, since the dependence of the true stress−strain curves on the strain rate is neglected, and rates greatly vary through the shoulder. For the LDPE sample, the true stress−strain curve does not exhibit a strain hardening. As a consequence, necking does not lead to a stable new equilibrium and the sample comes early to the point of fracture.

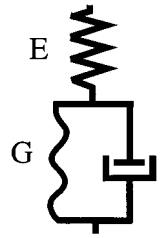

Figure 25. Haward−Thackray model for describing the deformation behavior of solid polymers.

4.3. Network Properties. The amorphous regions in partially crystalline samples such as polyethylene play a particular role in the deformation behavior. Chain sequences in these regions have their ends more or less fixed, either by the existing entanglements or by an anchoring in the adjacent crystallites. They thus set up a network, and this becomes stretched during the deformation process; the retractive forces resulting in the sample recovery originate from it. Stretching of the network means to increase and to store free energy. The work carried out on straining may thus be subdivided into a stored part and a dissipated part associated with the slip processes. Going from the solidlike HDPE to the rubberlike PEVA changes the weights of the two parts of the work. For HDPE at low strains, the dissipated part dominates the behavior. Only at large strains do network forces increase to a magnitude of similar order to the viscous forces. In PEVA, on the other hand, network forces are visible from the very beginning.

To learn more about the network properties, we follow the simple route devised by Haward and Thackray.[3] Long ago, they suggested that a partially crystalline polymer in its deformation properties could be represented by the model shown in Figure 25. The model includes three parameters, the initial tensile modulus E, the shear modulus of the network G, and a viscosity. Plots of σ versus $\lambda^2 - 1/\lambda$ yield two slopes, one at the origin, giving E, and the other at larger strains, giving G. The model is very simple, certainly too simple to represent correctly all the dissipative deformation modes. However, it can be successfully used for an extraction of the network properties, i.e., an estimate of G. Figure 26 shows such a Haward−Thackray plot, here for PEVA18. Curves may be separated into three linear regions before a final increase occurs. The interesting part is the central range located in the region of the activity of the slip processes. The slope gives the shear modulus, and we obtain $G = 2$ MPa.

From the order of magnitude, the result makes sense. For our sample which has a low crystallinity, we would expect a shear modulus not too far away from that measured in a polymer melt. Data given in literature somewhat vary, but they are all located in the range 1−2 MPa (compare, for example, Krigas et al.[34]). Carrying out the Haward−Thackray plot for all samples led us to the data given in Figure 27, showing the network shear modulus as a function of the degree of crystallization. One observes an increase with increasing crystallinity, essentially starting at the value of the melt. The increase is, of course, conceivable, considering that crystallites act in two ways, both as fillers and as cross-links, and both properties tend to increase G.

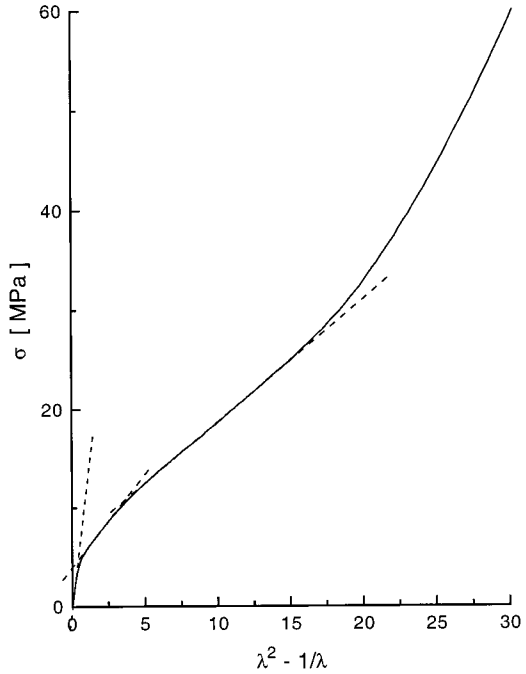

Figure 26. PEVA18: Haward−Thackray plot of the stress-extension dependence.

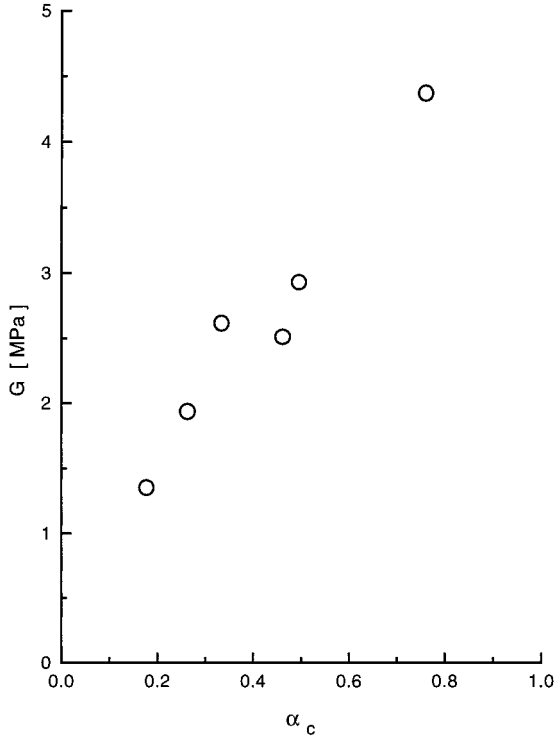

Figure 27. Network shear moduli of the various samples with different crystallinity as derived from the Haward−Thackray plots.

It is the entanglement network which preserves the memory of the original sample shape. For polymers with standard molecular weights, crystallization starting from the quiescent melt does not lead to a resolution of the existing entanglements. These are just shifted into the amorphous regions.[35] This means a redistribution on length scales of about 10 nm, but globally, the isotropic entangled network of the melt is retained. The isotropy is lost on straining the sample and reappears, with complete recovery, on heating. Entanglements rather than the crystallites represent the stable elements in a strained partially crystalline polymer for all samples, from the PEVAs to the HDPE. A loss of memory can only occur if entanglements are resolved, and thus, the network topology changes. For the samples under study, chain disentangling sets in at the point D, i.e., at a strain $\epsilon_H \approx 1$ (Figure 14). Surpassing this point also leads to a partial relaxation of the entanglement network, observed in the decrease of the amounts of recovery $\epsilon_{H,e}$ and $\epsilon_{H,s}$.

5. Conclusions

Our comparative studies on various polyethylenes lead to the conclusion that their deformation behavior under an applied tensile load has a common basis and is strain-controlled. Stress−strain curves may be split up into five different ranges and the transition points, where the differential compliance changes are, for all samples, located at similar values of the strain. Contrasting with the strains, the stresses at the cross-over point vary greatly, by more than 1 order of magnitude between the rubberlike PEVA 27 with a crystallinity of 18% and the solidlike HDPE (76% crystalline). In agreement with these findings, the textures of the crystallites are only strain dependent, commonly for all samples.

The observations tell us that the crystallites, although arranged in stacks of all orientations, are able to easily react on imposed strains in a well-defined unambiguous manner. Understanding this behavior appears difficult on the basis of the traditional views about the structure of polymer crystallites. In the large majority of the electron microscopic pictures of melt-crystallized polymers, these appear as continuous layers, being incorporated as stacks in spherulites. Recent studies on the mechanism of polymer crystallization, carried out on syndiotactic polypropylenes tend to modify the picture. Time-dependent small angle X-ray scattering experiments indicate that polymer crystallization is a two-step process, with the formation of crystalline blocks as a first step, and their incorporation into the final lamellar crystallite as a second step.[36,37] Lamellar crystals retain a memory of their history as they show a granular structure in AFM observations. In fact, this granular structure has also previously been observed in TEM pictures of, for example, low-density polyethylene,[38] but so far, this was considered as representing a peculiar property of this material. If blocklike substructures of the lamellae indeed constitute a general basic feature for all melt-crystallized polymers, the observed straightforward reaction to imposed strains becomes conceivable. Slip of blocks can take place on two slip planes, with two slip directions for each plane. Taken together with the interlamellar shear, which acts like a third slip system, again with two directions, we effectively have six independent slip systems, even more than is required (five) for accomplishing a general deformation for a multicrystalline system.[39] Surely, for PEVA, the observed (100) [001]-slips cannot be of the "fine" type, as they recover under the action of the weak network forces. Their magnitude is far below the critical resolved shear stress of 15 MPa cited by Young et al. as being necessary for the initiation of a homogeneous crystal shearing.[8] On the other hand, we find a common behavior in all samples and therefore conclude that the "coarse" block slip processes should be generally dominant. When occurring along the lateral (nonfolded) block surfaces, there might well exist a difference in the viscous forces arising for longitudinal (in chain direc-

tion) and transverse shifts. However, there is certainly no complete suppression of the latter processes. Furthermore, there could also exist a difference in the coupling of adjacent blocks along *b*, the direction of main growth of the lamellae, and along *a*.

Each block belongs to a certain lamella, up to point C, where this relation begins to get lost. Obviously, the amount of shear deformation which can be accomplished by the interlamellar amorphous layers is finite, as long as the lamella, although set together of displaced blocks, exist. On surpassing C, lamellae begin to disintegrate. In addition, the blocks cannot retain their identity. Under the action of the force, they can be completely reorganized, the new blocks being formed with the chain direction along the tensile axis. They provide cross-links, set at optimized positions, so that they allow, together with the entanglements, for the largest possible mobility of the fluidlike chain segments. The low apparent network shear modulus found in the third range of the Haward−Thackray plot of Figure 26 could be understood as indicating an ongoing network relaxation following from the restructuring.

Acknowledgment. Support of this work by the Deutsche Forschungsgemeinschaft (Sonderforschungsbereich 428 and Graduiertenkolleg "Strukturbildung in Makromolekularen Systemen") is gratefully acknowledged. Thanks are due to the "Fonds der Chemischen Industrie" for financial help.

References and Notes

(1) Capaccio, G.; Ward, I. *Colloid Polym. Sci.* **1982**, *260*, 46.
(2) Pakula, T.; Trznadel, M. *Polymer* **1985**, *26*, 1011.
(3) Haward, R.; Thackray, G. *Proc. R. Soc. A* **1968**, *302*, 453.
(4) Haward, R. *Macromolecules* **1993**, *26*, 5860.
(5) Termonia, Y.; Smith, P. *Macromolecules* **1988**, *21*, 2184.
(6) Cowking, A.; Rider, J. *J. Mater. Sci.* **1969**, *4*, 1051.
(7) Keller, A.; Pope, D. *J. Mater. Sci.* **1971**, *6*, 453.
(8) Young, R.; Bowden, P.; Ritchie, J.; Rider, J. *J. Mater. Sci.* **1973**, *8*, 23.
(9) Bowden, P.; Young, R. *J. Mater. Sci.* **1974**, *9*, 2034.
(10) Bartczak, Z.; Cohen, R.; Argon, A. *Macromolecules* **1992**, *25*, 4692.
(11) Bartczak, Z.; Argon, A.; Cohen, R. *Polymer* **1994**, *35*, 3427.
(12) Seguela, R.; Rietsch, F. *J. Mater. Sci. Lett.* **1990**, *9*, 46.
(13) Gerrits, N.; Tervoort, Y. *J. Mater. Sci.* **1992**, *27*, 1385.
(14) Petermann, J.; Schultz, J. *J. Mater. Sci.* **1978**, *13*, 50.
(15) Frank, F.; Keller, A.; O'Connor, A. *Phil. Mag.* **1958**, *3*, 64.
(16) Predecki, P.; Statton, W. *Jpn J. Appl. Phys.* **1968**, *7*, 31.
(17) Yamada, M.; Miyasaka, K.; Ishikawa, K. *J. Polym. Sci.* **1971**, *A-29*, 1083.
(18) Takahashi, Y.; Ishida, T. *J. Polym. Sci., Part B: Polym. Phys.* **1988**, *26*, 2267.
(19) Hay, I.; Keller, A. *Kolloid Z. Z. Polym.* **1965**, *204*, 43.
(20) Peterlin, A. *J. Mater. Sci.* **1971**, *6*, 490.
(21) Kanig, G. *J. Cryst. Growth* **1980**, *48*, 303.
(22) G'Sell, C.; Jonas, J. *J. Mater. Sci.* **1979**, *14*, 583.
(23) G'Sell, C.; Hiver, J.; Dahoun, A.; Souahi, A. *J. Mater. Sci.* **1992**, *27*, 5031.
(24) Bridgman, P. *Trans. Am. Soc. Met.* **1944**, *32*, 553.
(25) Hiss, R. Ph.D. Thesis, Freiburg, 1996.
(26) Polanyi, M. *Z. Phys.* **1921**, *7*, 149.
(27) Hasan, O.; Boyce, M.; Li, X.; Berko, S. *J. Polym. Sci.* **1993**, *31*, 185.
(28) Gauthier, C.; Perez, J.; Oleinik, E.; Rudnev, S.; Slavetskaya, T.; Kravchenko, M.; Salamatina, O. *10th International Conference on Deformation, Yield and Fracture of Polymers*; Institute of Materials: London, 1997; p 64.
(29) Fotheringham, D.; Cherry, B. *J. Mater. Sci.* **1978**, *13*, 951.
(30) Brooks, N.; Unwin, A.; Duckett, R.; Ward, I. *J. Macromol. Sci., Phys.* **1995**, *B34*, 29.
(31) Vincent, P. *Polymer* **1960**, *1*, 7.
(32) Strobl, G. *The Physics of Polymers*; Springer: New York, 1997; p 353.
(33) Bernstein, B.; Zapas, L. *J. Rheol.* **1981**, *25*, 83.
(34) Krigas, T.; Carella, J.; Struglinski, M.; Crist, B.; Graessley, W.; Schilling, F. *J. Polym. Sci.* **1985**, *23*, 509.
(35) Strobl, G. *The Physics of Polymers*; Springer: New York, 1997; p 143.
(36) Hauser, G.; Schmidtke, J.; Strobl, G. *Macromolecules* **1998**, *31*, 6250.
(37) Hugel, T.; Strobl, G.; Thomann, R. *Acta Polym.* **1999**, *50*, 214.
(38) Michler, G. *Ifunststoff-Mikromechanik*; Carl Hanser Verlag: Berlin, 1992; p 187.
(39) Kelly, A.; Groves, G. *Crystallography of Crystal Defects*; Longman: London, 1970.

MA981776B